The interplay between morphology and photocatalytic activity in ZnO and N-doped ZnO crystals

Byzynski, Gabriela[1]; Melo, Camila[2]; Volanti, Diogo P.[2]; Ferrer, Mateus M.[3]; Gouveia, Amanda F.[4]; Ribeiro, Cauê[5]; Andrés, Juan[6]; Longo, Elson[4]

(1) IQ, UNESP - Univ Estadual Paulista, Araraquara, SP, Brazil
(2) IBILCE, UNESP - Univ Estadual Paulista, S. J. Rio Preto, SP, Brazil
(3) FC, UNESP - Univ Estadual Paulista, Bauru, SP, Brazil
(4) DQ, UFSCar - Universidade Federal de São Carlos, São Carlos, SP, Brazil
(5) Embrapa Instrumentation, São Carlos, SP, Brazil
(6) Universitat Jaume I, UJI, Castelló, Spain

Abstract

Photocatalytic materials can perform oxidative and reductive reactions over their surfaces when excited with light. Intrinsic characteristics of the material such as superficial area, morphological structure, and crystalline phase exposition play a fundamental role in the corresponding reaction paths. However, especially in doped semiconductors, as ZnO:N, less is known about how the synthesis parameters affect the morphologies and the photocatalytic activity simultaneously. To solve this issue, ZnO and ZnO:N samples were obtained using microwave-assisted hydrothermal and modified polymeric precursor methods of synthesis. Samples morphologies were characterized by TEM and FE-SEM. Crystallographic phases were observed by XRD and optical characteristics by DRS. XPS results confirmed the doping process. Degradation of Rhodamine-B and Cr(VI) reduction were employed as probe reactions to investigate their photocatalytic activity. Although the crystallographic structure of these powders maintains the ZnO hexagonal wurtzite structure, the optical properties and morphologies, and photocatalytic activities present different behaviors. Also, density functional theory calculations were employed to determine the specific features related to electronic structure, morphology, and photocatalytic activity. Different synthesis methods produce a singular behavior in the physicochemical properties of materials, and the doping effect produces various modifications in RhB degradation and Cr(VI) reduction for each synthesis method. Crystal face exposition and morphologies are related to the improvement in the photocatalytic activity of the materials.

Keywords: DFT calculations; Semiconductor; Photocatalysis; Cr(VI) reduction; Rhodamine degradation.

1. Introduction

Zinc oxide (ZnO) is an important n-type semiconductor with a broad range of electric, gas sensing and photocatalytic properties with a band gap of 3.2 eV [1–6]. Therefore, many efforts have been made to synthesize ZnO-based semiconductors with different morphologies for specific devices, such as nanorods, nanobelts, nanosheets, microrod/microtube arrays, quantum dots and other complex hierarchical micro/nanostructures [7,8]. Synthetic routes to ZnO nanoparticles include modified polymeric precursor (MPP) [9], sputtering [10,11], hydrothermal [12], solvothermal[13,14], sol-gel [15,16], ultrasonic irradiation [17], microwave-assisted hydrothermal (MAH) [6,18,19], and zinc-precursor thermal decomposition with free-solvent [20,21] methods. The MPP method is one of the most common chemical synthesis of inorganic semiconductor materials due to its simplicity and low cost. Generally, for these synthesis methods, the heat treatment of the produced resin with elevated temperature is an essential step, resulting in the formation of particle aggregates. Hence, MPP method does not allow morphology control or size distribution, producing almost quasi-spherical particles, while MAH method is an easy, fast and principally inexpensive method in synthesized materials with enhanced properties. MAH methods demonstrate several advantages as one-step synthesis method with controlled size and shape since no high temperature, or high pressure is needed [22–25]. In particular, Niederberger et al. have shown that microwave-assisted nonaqueous sol-gel method is an efficient procedure for obtaining nanocrystalline metal oxides, including ZnO and transition metal doped ZnO nanoparticles, within just a few minutes [25].

To diminish the band gap of ZnO and, consequently, dislocate its light absorption spectrum into the visible region, non-metal doping of ZnO is considered as one of the most effective strategies to improve the photocatalytic activity. That approach avoids photo-generated holes and electrons recombination to obtain efficient photocatalyst materials, decreasing the quantum yield and causing energy dispersion [14,26–28].[7] Among non-metal elements, nitrogen (N) is the best choice, as it has nontoxicity and source abundance as well as its similar atomic radius, lowerelectronegativity, and ionization energy than the oxygen atom. N could be used to obtain a stable p-type N-doped ZnO (ZnO:N) semiconductor structure [29–31], resulting in the improvement of photocatalytic activity [32–41]. Theoretical calculations point out that N is the best superficial acceptor candidate for ZnO [42] while Amiri et al. [43] have analyzed the possible source of ferromagnetism in ZnO:N compounds by using *ab-initio* calculations. ZnO:N has been obtained by different routes, such as pulse laser deposition [44], molecular beam epitaxy [45], ion beam deposition [46] and sputtering [47–49]. Herring et al. [50] point out the synthesis of N-doped ZnO (ZnO:N) nanostructures through two different microwave irradiation methods which could control ZnO:N morphology and

doping level. Mendonça et al. [51][5] demonstrated that surface hydroxylation provokes an enhancement on the photocatalytic efficiency of TiO$_2$, confirming that the morphology and surface characteristics influence on the photoactivity. Very recently, our research group has presented a straightforward and fast method for the synthesis of ZnO:Nnanoparticles. The results allow the essential comprehension of the dye degradation mechanism associated with the photocatalytic activity of the generated p-type semiconductor [52]. Sudrajat and Babel [53] successfully synthesized ZnO:N and ZnO$_2$:N materials and compared the mechanism of their photocatalytic activities for the degradation of Rhodamine 6G. From these works, it is possible to conclude that not only specific surface area, band gap values, mid-gap energetic levels (energetic inner levels) created by the doping process influence the photocatalytic activity of materials, but also morphology plays a major role in defining the semiconductor properties. Another strategy to diminished the band gap values is the uses of heterostructures or composites of different band gap semiconductors [54–57], resulting in an efficient separation of charge carriers.

This study seeks to fulfill a two-fold objective. Firstly, find a relationship between the morphology and photocatalytic activity (degradation of Rhodamine-B and Cr(VI) reduction) of 3D flower-like ZnO and ZnO:N powders synthesized by both MPP and MAH methods. Secondly,employ the first principle calculations, based on density functional theory, to obtain a little interpretation of the morphology changes as a function of the relative stability of the surfaces. The paper is presented as follow: first, introduces the synthesis methods and characterization techniques for the ZnO and ZnO:N, as well as the calculation method and models. In section 3, the results are shown and discussed. Finally, the key findings are outlined in section 4.

2.   Materials and Methods
2.1.   Synthesis of ZnO and ZnO:N

The samples were synthesized by two different methods: MPP and MAH. Using MPP method, a ZnO resin was obtained similarly to previously work [52] by dissolving zinc acetate (Zn(C$_2$H$_3$O$_2$)$_2$ – Sigma-Aldrich) in monohydrated citric acid (C$_6$H$_8$O$_7$.H$_2$O Sigma-Aldrich) solution, in a molar ratio 1:1. After that, the mixed solution was magnetically stirring during 10 minutes. With the citric acid addition, the solution pH was controlled to avoid the Zn(OH)$_2$ precipitates and for the Zn^{2+} stays homogeneous dispersed in the solution. The ZnO resin obtained was calcined at 130 ºC for 4 h, to solvent elimination; and, then, to 600 ºC for more 4 h. The gravimetric analysis quantified the concentration of 12.29 mol L^{-1} for ZnO resin. For the doping process, urea (CH$_4$N$_2$O – Sigma-Aldrich) (5% molar ratio) was dispersed in the

resulted solution of zinc acetate and citric acid, before the heat treatment. After urea addition, the samples acquiesced to the heat treatment similar to previously described. In this way, the undoped sample was named as ZnOp and doped N sample labeled as ZnO:Np.

For the MAH method, 60 mL of zinc acetate solution (17 mmol L^{-1}) was strongly stirred and, after 10 min, 10 mL of NaOH solution (2 mol L^{-1}) (Synth) was added. The ZnO resin was inserted into a Polytetrafluoroethylene (PTFE) hydrothermal reactor for 1 h and at 100 °C assisted microwave-aided device for hydrothermal synthesis (800W) [58]. The N-doped sample was obtained adding urea (5% molar ratio) before the NaOH solution addition and under the same MAH reactions condition used for the undoped sample. The undoped sample was named as ZnOm and doped N sample as ZnO:Nm.

2.2. Characterization techniques.

Diverse techniques characterized the samples obtained. The morphology and size of the powders were described by field emission scanning electron microscopy (FE-SEM) (JEOL Microscope Model JSM 6701F) and transmission electron microscopy (TEM) (FEI microscope, model Tecnai F20).

To evaluate crystalline phase structure, X-ray dispersion (XRD) (Miniflex 300 Rigaku) was employed with a Cu anode ($\lambda Cu-K_\alpha$ = 0.154 nm) in the range of 2θ = 20–70 ° at 2 ° min^{-1} step. N_2 physisorption (Micromeritics Gemini VII) was used to obtain the surface areas (SA) of synthesized samples, using the Brunauer-Emmett-Teller (BET) method.

The optical properties evaluation was done using UV/vis diffuse reflectance spectrophotometer (UV– vis–NIR Cary 5G spectrophotometer) (DRS) and fluorimeter spectrometer (Perkin Elmer, model LS50B) (PL). X-ray photoelectron spectroscopy (XPS) (Thermo K-Alpha XPS Thermo Scientific, Inc.) were used to evaluate nitrogen doping level with radiation of Al K_α, under vacuum condition and 400 μm spot size. The Survey spectra resolution was 1 eV with 10 scans, and higher resolution spectra were 0.1 eV with 50 scans.

A crystal assumes an equilibrium shape determined by the calculations from Wulff construction where the total free energy at a fixed volume is minimized, and the surface energy, E_{surf} of an (hkl) plane is related to the distance from the center of the crystallite in the normal direction[59]. Similar equilibrium morphology models obtained based on the calculations realized by Na and Park [60] allowed the estimation of the surface energies of the particles, under the condition that crystal faces with lowest surface energies govern the crystal morphology. These results can be used to explicitly predict the evolution of morphologies in different environments, as recently developed by our research group [61,62].

In this work, simulation considering the energy modulation of the (110), (100), (101), (001) (102), (112) and (111) faces of ZnO, starting from the E_{surf} previously calculated by Na and Park [60], were conducted based on the Wulff equation. Therefore, the assumption of the ratio modification between the E_{surf} for each surface shows the paths of morphological changes. Results allowed a combination of experimental and theoretical insights into electronic, structural, and energetic properties, which enable the morphology and transformation mechanisms control. The Visualization for Electronic and Structural Analysis (VESTA) program has been utilized to obtain the morphologies [63].

2.3. Photocatalytic procedures

The photocatalytic activity of semiconductor materials was evaluated measuring the discoloration of Rhodamine-B (RhB) (2.5 mg L^{-1}) dye solution. 2 mg of samples were dispersed in 20 mL of RhB solution, in a separate beaker for each sample, under magnetic stirring. The solutions were then illuminated with six UVC lamps (TUV Philips, 15W, with maximum intensity at 254 nm), during 2 h, under magnetic stirring at a constant temperature of 25 ºC, and aliquots of each solution were taken every 30 minutes. A UV–vis spectrophotometer (Shimadzu-UV-1601 PC spectrophotometer) was used to monitor modifications in the optical absorption of RhB from the resulted solutions throughout the experiment. Similar procedure was repeated using a visible light source (six Philips lamps, 15W, and maximum intensity at 440 nm). Control, without the semiconductor materials, was also performed (photolysis). The kinetic results presented in the manuscript are an average of three experiments, and it showed the standard deviations for each measurement in defined time reaction. It also showed the standard deviations for kinetic rates, as the R-squared.

The photocatalytic activity was also evaluated for Cr(VI) reduction. All experiments were carried out using 15 mL of 1 mg L^{-1} Cr(VI) solution, in a separated beaker, ($K_2Cr_2O_7$ - SpecSol) and 1.5 mg of each ZnO samples. The suspensions were stirred under UV illumination (TUV Philips, 15W, with maximum intensity at 254 nm) for 2 h, being the aliquots obtained every 30 minutes. The suspensions were separated by centrifugation at 3500 rpm for 15 min. Control, without the semiconductor materials, was also conducted. Cr(VI) concentration was determined by spectrophotometry at 540 nm using the diphenyl carbazide method [64]. Cr(III) concentration was calculated by the difference between Cr Total and Cr(VI), being the Cr Total determined by graphite furnace atomic absorption spectrophotometry (GFAAS) (Varian, AA280Z). The pH was monitored at the beginning and the end of all experiments. All experimental data are based on the average of triplicate.

3. Results and Discussion

3.1. FE-SEM, TEM, and Morphological Analysis

FE-SEM images (Figure 1A, 1C, 1E, 1G) of ZnO samples, obtained by MAH synthesis, indicate no significant influence of doping on the particle morphology. Both materials, undoped ZnOm and doped ZnO (ZnO:Nm), show mainly hierarchical flower-like structures, which have an array of oriented nanorods. For the undoped sample (ZnOm) (Figure 1A), the rods are 1.2 - 1.7 μm in length with an approximate diameter of 0.1 μm. N-doping (ZnO:Nm) promoted an increase in the particle length (Figure 1C) to 2.0 - 2.4 μm, due to urea which could stimulate the ZnO crystal growth owing to the decrease in pH of the precursor solution.

Ahmed et al. [65] [14] presented a growth mechanism of ZnO nanostructures in basic aqueous solution, in which this process occurs in two-step: nucleation and growth. The first step of the mechanism is the dissociation of a basic salt with Zn^{2+} precursor, which then reacts with OH^- groups to form $Zn(OH)_2$ and later into $[Zn(OH)_4]^{2-}$. This ion is responsible for the formation of ZnO crystals with water and OH^- anions. Positively charged Zn-(0001) and negatively charged O-(0001) surfaces forms a ZnO wurtzite crystal, defining polar surfaces [65,66].[17,36] At the nucleation stage, the high amount of OH^- groups promotes an equilibrium shift, endorsing the crystal growth along [0001] or c-axis direction. This mechanism confirms the crystal growth of MAH samples and, especially, the larger size of ZnO:Nm sample compared to ZnOm, due to the mostbasic medium of the aqueous precursor solution, pH ~12. The crystallographic habit of ZnO, on which the 1D growth process takes place along the (0001) surface, is observed with subsequent appearance of nanorods, as it has been reported by other authors [65].[17] For both samples, ZnOm and ZnO:Nm, it is possible to observe a polished surface with a hexagonal cross-section with an extremity of nanorods a six-fold pyramidal geometry.

Samples obtained by MPP method (ZnOp and ZnO:Np) (Figure 1E, 1F) exhibit a predominant hexagonal morphology (nanoplates) without a significant variation due to the doping process. There is a different size distribution of the undoped (ZnOp) and doped (ZnO:Np) samples, with an average size of smallest particles of 50–60 nm and largest particles of 110–140 nm. Doping process does not affect even particle size. The morphology of the resulted materials synthesized by MPP method is similar to with other authors using the same synthetic method [52].

The high-resolution transmission electron microscopy (HRTEM) of MAH (Figure 1B, 1D) and MPP samples (Figure 1F, 1H) confirms the microstructural morphology and size presented by FESEM images. For MAH samples, HRTEM shows that ZnOm rods (Figure 1B)

are crystalline structures, with a lattice spacing of about 0.28 nm. The doping process does not modify the lattice spacing of ZnO:Nm sample (Figure 1D), which is 0.28 nm. These lattice spacing correspond to the distance between the (002) planes, implying that the c-axis ((001) direction) is the preferential growth direction of ZnO crystals in MAH conditions synthesis [19].

For MPP samples (Figure 1F, 1H), HRTEM images depict that ZnO particles with an average size 50-60 nm are formed by singles crystals specimen with an average size of 5-15 nm. The thickness thinner than MAH samples characteristics results in highly crystalline material, with anadjacent lattice spacing of about 0.30 nm, which corresponds to the interspacing of the (101) planes of ZnO lattice [67].

The main difference between the morphological parameters of the nanoparticles obtained by MPP and MAH methods are associated with the growth mechanisms. Due to the polymerization process, precursor pH solution and calcination step, the first method delimits the nanoplate particles with reduced size. Instead, the second method provokes an anisotropic particle growth due to the OH⁻ disposal in the reaction media, promoting crystal growth along the c-direction. This morphological difference is the origin of the different photocatalytic activities.

The crystals morphologies and growth direction were studied using the theoretical Wulff construction obtained through the values of the surface energies reported by Na and Park [60][12] and is depicted on the left of Figure 2. Initially, the Wulff crystal shows five exposed surfaces. However, the same morphology is entirely different from MAH synthesis, especially because of the OH⁻ ions concentration in the precursor solution, since in MPP synthesis, the pH is around 5. In this case, the crystal growth along [0001] is inhibited {(110), (100), (101), (001) and (102)} of the seven calculated by Na and Park[12] {(110), (100), (101), (001) (102), (112) and (111)}. The simulated structure represents the typical morphology in a *vacuum*. The experimental morphologies are different from the typical morphology because it does not take into account the specific interactions as well as the defects present along the synthetic route.

A simple method is applied to circumvent these drawbacks by tuning the ratio between the values of surface energies to find the morphology transformations. In this sense, the stabilization of (100) surface on the (101) surface (**¡Error! Nombre de archivo no especificado.** in the typical morphology to **¡Error! Nombre de archivo no especificado.**) results in a hexagon morphology with the (100) and (001) exposed surfaces, the same obtained for the ZnOp and ZnO:Np samples. With this relation, the (100) overlapped the (110), (101) and (102) surfaces. It would also be possible to create a hexagon by stabilizing the (110) surface that would overlap

the (100) surface, as it was previously reported from the results obtained by transmission electron microscopy [17]in which ZnO hexagons are formed by the (100) surface [65]. Accordingly, along the synthesis of the MPP method, a stabilization of the (100) and (001) surfaces take place.

In the case of the ZnOm and ZnO:Nm samples, the six-fold pyramidal geometry is obtained by the stabilization of the (101) and (102) surfaces. Figure 3 shows the result of the stabilization of the (101) and (102) surfaces starting from the hexagon morphology. Furthermore, the angles formed with the (100) surface determine the surface of the experimental nanorods, as seen in Figure 2. This result suggests that the (101) surface in which the experimental and theoretical angle between the morphologies coincides forms, the six-fold pyramidal geometry observed.

Another interesting point in this analytical tool is the possibility to study the particle length variation. In the MAH synthesis, there was a particle enlargement due to the presence of the dopant. It is necessary to modify the (100)/(101) ratio to improve the enlargement, in this case, the destabilization of the (101) surface. Thereby, the exposed area of the (101) surface becomes smaller than (100) surface, resulting in a long nanorod (see Figure 1). For this purpose, it is also necessary to increase the E_{surf} of other surfaces to maintain the (101) surface exclusively. This fact shows that the pH solution or dopant causes major modification of the surface extremities, making them more unstable than (101) surface. Based on the same reasoning, flattening in the c-direction of the hexagons was obtained by MPP synthesis, about the particles of MAH synthesis,representing the higher stability of (0001) surface, and hence a larger exposure.

3.2. Material Characterization

X-ray diffraction (XRD) was used to identify the crystalline phase structure of all samples. Figure 4A is a representative XRD pattern obtained, and all ZnO diffraction peaks were well indexed to the ZnO hexagonal wurtzite structure (JCPDS 36-1451), confirming that thesynthesized semiconductors were single-phase materials. Neither doping nor synthesis method alters the wurtzite phase crystallographic structure, being possible to observe no new peaks of impurities. Figure 4B confirms a slight difference between XRD peaks after the doping process, indicating a modification in ZnO lattice.

Table 1 presents the specific surface areas (SSA) obtained by the BET isotherms method for the synthesized samples. The undoped sample prepared by MPP (ZnOp) present lower SSA than the doped one (ZnO:Np). Considering MAH samples, the behavior is opposite, the

undoped sample (ZnOm) present a higher SSA than the doped one. However, it is clear that MAH samples show an increase in SSA compared with MPP samples.

The SSA results for MPP samples corroborate with agglomeration formation, a typical feature for materials obtained by the MPP method. The SSA results collaborate with FE-SEM results in the sense that MAH samples indicate more elevated SSA than MPP samples. MAH and MPP samples present unique morphologies that are defined by the crystallization method, i.e., calcination in MPP and hydrothermal annealing in MAH, which reflects in the material SSA. In MAH samples, the crystallization happens in liquid environment, where the urea effect is limited to the in situ formation of electrolytes, e.g., NH_4^+. Then, during this process the electrokinetic equilibrium changes, tending to particle agglomeration that may explain the reduced SSA values in doped samples. On the other hand, MPP is crystallized by thermal treatment in air, where crystal growth will be limited by solid-state interface. Then, in that case the presence of higher organic fractions may hinder the growth by covering effect, which is also known in calcination of high C-content samples [68]. Then, without solid-state interfaces the crystal growth is avoided and consequently, SSA values tend to increase.

Diffusive reflectance spectroscopy (DRS) was utilized to observe the influence of N-doping on the optical characteristics of ZnO synthesized samples. Figure 5 presents the Kubelka-Munk relation [69] used in estimating the band gap value of ZnO samples. For ZnOp and ZnO:Np,synthesized by MPP method, the optical absorbance behavior between the undoped and doped samples changed slightly, indicating that N-doping process alters optical behavior. The band gap value obtained with a straight line crosses the energy (eV) axis, as presented in Figure 5 and shownin Table 1. The band gap values performance indicates that N-doping process does not modify the band gap value as presented in a previous report [15][8], but the applied synthesis method influences more in the band gap alteration, due to the different growth mechanisms of ZnO particles for each method and consequently the resultant morphology. It is conclusive that the energetic intermediate levels formed between the conduction and valence band do not drastically change the band gap value.

The density of states of N-doped ZnO nanoparticles showed that the substitutional nitrogen does not vary the intrinsic band gap related to (0110) surface, but the local states of N 2p show as mid-gap level (inter energy level), between valence and conduction band of ZnO[41]. This result is evidence that N-doping process does not modify the band gap values drastically [70].

X-ray photoelectron spectroscopy was conducted to confirm the N-doping in both different synthesis methods. The reference for spectra is C 1s line. Figure 6A shows similar Survey spectra of all samples, indicating that the principal elements are zinc and

oxygen. It is not possible to identify N binding energy peaks in the high-resolution spectra, due to the low percentage of the element in the material synthesized. High-resolution spectra for Zn 2p, O 1s, and N 1s are presented in Figure 6 A, 6B, and 6C, respectively. ZnO characteristic energy peaks are observed in Zn 2p core level spectra for all samples of 1020.4 – 1020.3 eV (Zn 2p$^{3/2}$) and 1043.5 – 1043.6 eV (Zn 2p$^{1/2}$) [71]. There is no displacement in binding energy when N is inserted in the ZnO lattice, indicating no Zn–N bonds, indicating that the N presence is in the interstitial sites in the ZnO lattice.

O 1s core level spectra present three energy peaks (Figure 6) fitted by Gaussian deconvolution to obtain three peaks. The first deconvoluted energy peak at 529.1 - 529.3 eV corresponds to the characteristic hexagonal wurtzite Zn-O binding energy. The second one, at 530.9 - 531.4 eV, is related to the C = O binding energy of carbon dioxide adsorbed on the material surface, and, finally, at 530.1 - 530.4 eV, indicating the oxygen vacancies (V_o) in the ZnO structure [72]. When the samples are doped, O 1s spectra present a displacement in the binding energy in lowest energy peaks, confirming the modification in Zn-O bonds caused by doping, and, in the energy peaks corresponding to oxygen vacancies. Doping promotes the insertion of N ion in the ZnO lattice, as an interstitial or substitutional state, and increase the oxygen vacancies. ZnO:Np sample shows new energy peak in O1s core level spectra at 534.89 eV, indicating the presence of urea energy bonds, as urea is a precursor in the synthesis methods. N 1s core level confirmed the presence of N in ZnO:Np and ZnO:Nm samples, indicating by a characteristic energy peak at 398.23 – 398.04 eV, similar to presented for N-doped ZnO in the literature [52].

Based on XPS technique, it estimated the valence band edge (Figure 6E), and the band gap structure (insert Figure 6E) of samples [73]. The conduction band (CB) and valence band (VB) energy values of doped samples (ZnO:Nm and ZnO:Np) are clearly more positive compared to undoped one (ZnOm and ZnOp), which confirmed the effect of N-doping in ZnO [74]. In this case, beyond the doping process promotes the creation of inter-band between CB and VB promoted by oxygen vacancies during the N doping process, which increase the light harvesting, mainly in the visible region [72,75], N doping process modify the VB and CB edge.

3.3. Photocatalytic activity for Rhodamine-B dye

Figure 7 shows the photocatalytic activity of ZnO samples obtained by MAH (ZnOm and ZnO:Nm) and MPP (ZnOp and ZnO:Np) for dye (Rhodamine-B) degradation under UV and visible illumination. It is important to note that aqueous solution discoloration supposed dye degradation during illuminating. From the curve decay observed for Rhodamine-B, it was

It is possible to observe that all ZnO samples present photocatalytic activity in this condition, although samples synthesized by MAH method present an impressive increase in photocatalytic activity compared with samples obtained by MPP. Table 2 presents the kinetic rates (k') normalized by the superficial area results of RhB discoloration for MPP and MAH samples, under UV and visible illumination, respectively, which considered the first order of RhB concentration. The kinetic rates (k) for each sample were obtained considering the reaction velocity dependent to the Rhodamine B concentration in different time reaction ([RhB]) and active sites ([AS]) where Rhodamine-B adsorbs to occur the discoloration reaction, as demonstrated in Equation 1.

$$v = -d[RhB]/dt = k[RhB][AS] \tag{1}$$

Active sites are constant for determined samples and could be related to the superficial area of each sample. Consequently, [AS] is incorporated into kinetic rate (k). The integration of kinetic law allows to obtained k' values as described in Equation 2:

$$-ln\ [RhB]/[RhB]_0 = k't \tag{2}$$

The modification in photocatalytic activity as a function of the synthetic method is due to two main factors: i) well-designed morphology and ii) active semiconductor surface. The active semiconductor surface is related to the superficial surface area values and, the photocatalytic degradation is classified as surface-dependent processes as occurs on the surface of ZnO. In this way, the rate constant for Rhod discoloration are normalized by surface area (Table 2), and only the morphology influences are taken into account. Related to the first factor, the movement of photoinduced carriers (electrons and holes) to the ZnO surface could induce recombination reactions, making all processes inactive. For carrier migration to occur, an appropriate concentration gradient or potential gradient, which is closely related to the morphology surface structure characteristics of ZnO, is crucial. So the exposed ZnO crystal facets are decisive in defining the photocatalytic activity [76]. [19]

ZnOm and ZnO:Nm samples display a non-similar morphology characteristics compared with ZnOp and ZnO:Np samples (Figure 1). ZnOm and ZnO:Nm samples are an array of oriented nanorods, which may inhibit the carrier´s recombination better than the ZnOp and ZnO:Np, made of nanoplate particles with different size. The photocatalytic process was efficient for MAH samples because it promotes less electron/hole pair recombination (Figure S3). Apart from recombination effect, it is evident that MAH method promotes nanorods particles formation with the major crystal faces with an exposition of (002) surface, due to

anisotropy growth mechanism. Compared to MPP method, which formed nanoplate particles with the preferred (101) crystal faces exposition, it is possible to conclude that crystal face exposition tightly influences photocatalytic activity. Also, by comparing (002) and (101), the first one presents an increase in photocatalytic activity for RhB discoloration, during UV illumination. The influence of photocatalytic activity by crystal face exposition is observed by other authors [77–79].[44,45] The specific surface area (SSA) of ZnOm is higher than ZnO:Nm sample, promoting the increase in photocatalytic activity under UV illumination. Even though the band gap value does not change (3.21 for ZnOm and 3.22 eV for ZnO:Nm), the recombination rate increases (PL results in Figure S3) in the doped sample, caused by the intermediated levels created for N-doping, resulting in UV photocatalytic activity reduction. In this way, the N percentage in this method synthesis could be considered elevated [52,80,81].[30,46,47] Sudrajat and Babel [53] confirmed that adsorption of Rhodamine 6G on the ZnO:Nmaterials surface is the rate determining step in the degradation mechanism. In this way, SSA and the availability of surface functional groups play a crucial role in the photocatalytic activity of ZnO:N. Moreover, the same authors showed that highly oxidative hydroxyl radicals are principallyresponsible for Rhodamine 6G degradation under UV light. On the other hand, superoxide radical and singlet oxygen which is classified as less oxidative reactive species play a major role in Rhodamine 6G mechanism degradation under visible light [53].

Through the RhB photocatalytic degradation in the presence of some scavenger solutions under UV illumination (Butyl alcohol, p-benzoquinone, and EDTA solution) and visible illumination (Butyl alcohol, p-benzoquinone, and silver nitrate), it is possible to confirm the influence of main activated oxygen species on degradation mechanism [82–84]. Under UV illumination (insert in Figure 7A), the directly photo-oxidation of RhB with structure oxygen vacancies (V_o)/holes influences directly the ZnOm and ZnO:Nm samples mechanisms. Although, OH* and O_2H* play a major role in the RhB degradation mechanism (insert Figure 7A), being also important for RhB discoloration reaction. The oxygen vacancies quantity in MAH samples is more elevated than MPP samples [19,24,85] (FTIR results in Figure S2, and PL results in Figure S3), which modifies the RhB degradation mechanism, improving the MAH photocatalytic efficiency.

Based on cluster model, 4-folder tetrahedron ($[ZnO_4]^x$) constitutes the ZnO structure and $[ZnO4]^x$ associates with neutral (V_o^x) or mono-ionized ($V_o^\bullet$) or di-ionized ($V_o^{\bullet\bullet}$) oxygen vacancies. When the ZnO particles ($[ZnO_4]^x$) absorb light of wavelength shorter than around 388 nm, electrons in VB are then photo-generated ($[ZnO_4]'$) to CB, forming holes in VB ($[ZnO_3.V_o^\bullet]$). The both charge, electrons, and holes, quickly reach the material surface to

instigate redox reactions [52]. Holes on the material surface can promote reactive oxidants as hydroxyl radicals, and the most reduction processes (O_2 reduction to superoxides radicals, H_2 generation, chromium (VI) reduction) can be initiated by electrons photo-generated. The increase in oxygen vacancies in MAH samples is closely related to the higher surface hydroxylation promoted by microwave synthesis method [86] (Figure S2 and S3) and differs from MPP samples, as discussed by Silva et al. [52], as described:

$$[ZnO_3.V_o^\bullet]...OH_2(ads) \rightarrow [ZnO_3.V_o^x]...OH^*{}_{(ads)} + H^\bullet$$
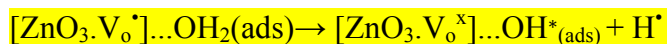
Moreover, the O_2H^* production increases compared with MPP samples.

$$[ZnO_3.V_o^\bullet] + O_2 \rightarrow [ZnO_3.V_o^\bullet]...O_{2(ads)} \rightarrow [ZnO_3.V_o^{\bullet\bullet}]...O_2{'}_{(ads)}$$

$$[ZnO_3.V_o^{\bullet\bullet}]...O_2{'}_{(ads)} + H^\bullet \rightarrow [ZnO_3.V_o^{\bullet\bullet}]...O_2H^*{}_{(ads)}$$
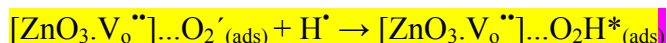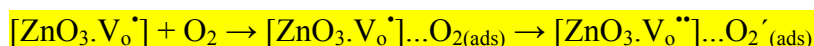
Figure 7B shows the photocatalytic activity of ZnO samples obtained by MPP and MAH methods for RhB degradation under visible illumination. Similar to UV illumination (Figure 7A), MAH nanorods particles evidently display better RhB discoloration compared with MPP nanoplates samples. Under this condition, factors that influence UV photocatalytic activity to take place also under visible illumination, such as crystal face exposition, morphology, and band gap values. Another important element that affects is a dye-sensitizing mechanism, which is particular to colored materials degradation. As the energy absorption occurs in colored material, an electron is easily excited and transferred to the ZnO energetic bands, promoting an increase in charge carrier separation (Figure S3). Therefore, visible photocatalytic activity will be increased [15]. [8]

Under visible illumination (Figure 7B), the recombination rate also occurs, in less proportion than under UV illumination and the effect of SSA is considered. For MAH samples, the influence of doping process in the photocatalytic activity under UV illumination is negative. In other words, ZnO:Nm presents lower UV photocatalytic activity than ZnOm sample. Although, it is important to notice the effect of dye-sensitizing mechanism, which could spread the photocatalytic activity, resulting in the same k' values for undoped and doped MAH samples under visible illumination.

Compared with MAH samples, where the N doping does not display an effective improve the photocatalytic activity, the MPP samples presents an opposite behavior. Under UV illumination (Figure 7A), ZnO:Np sample shows a major increase in RhB discoloration compared with ZnOp sample, which could be related to SSA values, once the SSA of ZnO:Np is higher to the SSA of ZnOp. N percentage in doping process for MPP samples are considered appropriate to enlarge the electrons/holes pair's creation and charge carrier separation, resulting in a UV photocatalytic activity enhancement. Under visible illumination (Figure 7B and Table 2), ZnO:Np also shows an increase in RhB discoloration, confirming that

intermediated energetic levels created by the N doping process are efficiency in promoting a modification in radicals production (insert Figure 7B), resulting in a better photocatalytic activity. It is important also, to consider that the dye-sensitizing mechanism under RhB discoloration, even though it is not possible to quantify the exact proportion of each event in all process only with the presented results. For MPP method, the N percentage is considered adequate to obtain higher photocatalytic activity under UV and visible illumination.

The insert of Figure 7B shows the main radical involved in RhB degradation mechanism for MAH samples, indicating that the main radical in the cited reaction is O_2H* for ZnOm sample, and for doped sample (ZnO:Nm), being the O_2H* radical as oxygen vacancies/holes crucial. The intermediated energetic levels created between CB and VB through doping effect affects the RhB degradation mechanism though does not increase photocatalytic efficiency under visible light. MPP samples described by Silva et al. [52] show the major radical responsible for RhB degradation as OH*, differs from MAH samples, confirming that the mechanism sample affects the physicochemical properties of materials, as photocatalytic radical production and efficiency.

3.4. Photocatalytic reduction of Cr(VI)

It was also investigated the photocatalytic activity related to the reduction of Cr(VI) to Cr(III) using ZnO synthesized samples. Figure 8 shows the reduction of Cr(VI) in function of illumination time without semiconductor and with ZnO samples. The formation of Cr(III) resulted by the Cr(VI) reduction is presenting in Figure S4. Similar to Rhodamine degradation mechanism (Figure 9A), ZnO particles photo-generation charges were generated when ZnO particles absorb light (Figure 9B). There is no adsorption of Cr(VI) in dark conditions in surface materials. Electrons in CB are then photo-generated ($[ZnO_4]'$) and are forming holes in VB ($[ZnO_3.V_o^\bullet]$). The both charge quickly reach the surface material to instigate redox reactions. In this way, the oxidation and reduction abilities of trapped electrons and holes are directly reliant on CB and VB positions. Holes on the surface material promote reactive oxidants as hydroxyl radicals, resulting in the initiation of the most reduction processes (O_2 reduction to superoxides radicals, H_2 generation, chromium (VI) reduction) by photo-generated electrons. In this way, the Cr(VI) reduction occurs in a directlyway, when photo-electrons from ZnO particles reduce Cr(VI).

A negligible self-reduction of Cr(VI) can be verified without semiconductors (<10%) in Figure 8, while a negligible self-formation of Cr(III) (Figure S4) follows the reduction of Cr(VI). Kieber and Helz [87] reported that irradiation could start reduction of Cr(VI). The decrease of Cr(VI) is the photocatalytic reduction, once the adsorption of Cr(VI) is unlikely
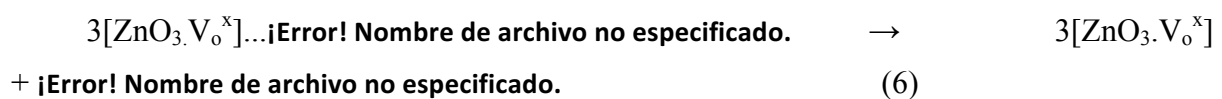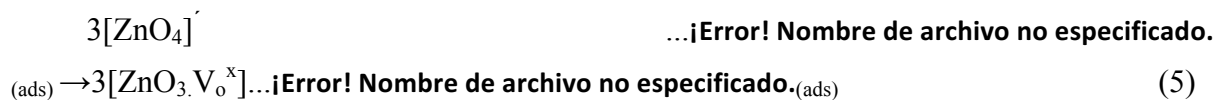
due to electrical repulsion between $Cr_2O_7^{-2}$ and negatively surface charge of ZnO. Shao et al. [88][22] observed the same behavior for Cr(VI) without any materials added.

The presence of ZnO samples shows an influence on the reduction of Cr(VI). Comparing the two synthesis methods, the samples obtained by MAH method reduced 45% and 75% of Cr(VI) for ZnO:Nm and ZnOm, respectively, while the MPP as-synthetized samples degraded 15% of Cr(VI) for both ZnOp and ZnO:Np. The main difference observed between the two synthesis methods is the specific surface area and the morphology. For MAH samples, the SSA is four times higher than for MPP samples, which could explain the higher reduction of Cr (VI) for ZnOm andZnO:Nm (Figure 8, Table 2). A slight difference in the SSA is also observed between undoped and doped MAH samples, being the undoped higher than the doped samples, justifying the 75% of reduction of Cr (VI). As mentioned above, the morphology is hierarchical flower-like structures for ZnOm and ZnO:Nm and hexagonal structures for ZnOp and ZnO:Np. Song et al. [89] observed a degradation efficiency of 29% and 95% of Cr(VI) for ZnO samples with hierarchical flower-like morphology and crew-like morphology, respectively. In the literature, sheet-like and butterfly-like ZnO nanostructures samples degraded more than 95%, and this behavior is due to the specific surface area [90].
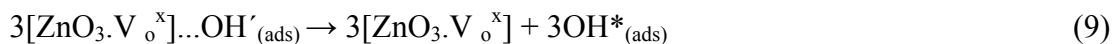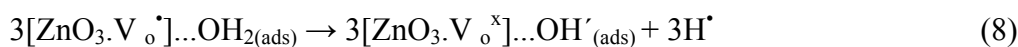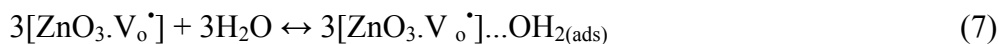
Based on cluster model, the reduction mechanism of Cr(VI) is illustrated in Figure 9B, where the magnitude and structural order-disorder effects regulate the materials properties [52][30]. In the beginning, $[ZnO_4]^x$ is associated with neutral (V_o^x) or mono-ionized ($V_o^{\bullet}$) or di-ionized ($V_o^{\bullet\bullet}$) oxygen vacancies and, with a photon incident, promote a $[ZnO_4]'$ (negative charge or electron promotion) and $[ZnO_3.V_o^{\bullet}]$ (positive charge or hole formation) creation (Figure 9B e 9C), as shown by the Equation 3.

$$[ZnO_4]^x + [ZnO_3.V_o^x] \rightarrow [ZnO_4]' + [ZnO_3.V_o^{\bullet}] \tag{3}$$
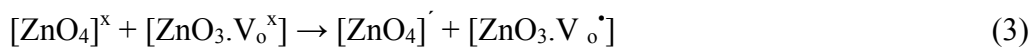
In situation 1, redox reactions with dichromate **¡Error! Nombre de archivo no especificado.**) species and $[ZnO_4]'$ cluster consequently occur, forming reduced chromium species **¡Error! Nombre de archivo no especificado.**) and $[ZnO_3.V_o^x]$ cluster, as demonstrated in the Equations 4, 5 and 6.

$$3[ZnO_4]' + \text{¡Error! Nombre de archivo no especificado.} \leftrightarrow 3[ZnO_4]' ...$$
¡Error! Nombre de archivo no especificado.$_{(ads)}$ (4)

$$3[ZnO_4]' ...\text{¡Error! Nombre de archivo no especificado.}$$
$_{(ads)} \rightarrow 3[ZnO_3.V_o^x]...\text{¡Error! Nombre de archivo no especificado.}_{(ads)}$ (5)

$$3[ZnO_3.V_o^x]...\text{¡Error! Nombre de archivo no especificado.} \rightarrow 3[ZnO_3.V_o^x]$$
+ **¡Error! Nombre de archivo no especificado.** (6)

At the same time, reaction between $[ZnO_3.V_o^\bullet]$ cluster and water molecule happen, creating hydroxyl radicals (Figure 9B<mark>), as described in the Equations 7, 8 and 9.</mark>

$$3[ZnO_3.V_o^\bullet] + 3H_2O \leftrightarrow 3[ZnO_3.V_o^\bullet]...OH_{2(ads)} \tag{7}$$

$$3[ZnO_3.V_o^\bullet]...OH_{2(ads)} \rightarrow 3[ZnO_3.V_o^x]...OH'_{(ads)} + 3H^\bullet \tag{8}$$

$$3[ZnO_3.V_o^x]...OH'_{(ads)} \rightarrow 3[ZnO_3.V_o^x] + 3OH*_{(ads)} \tag{9}$$

Another situation, named as situation 2, is induced for mono-ionized oxygen vacancies ($[ZnO_3.V_o^\bullet]$) and **¡Error! Nombre de archivo no especificado.**) species. In this case, instead of hydroxyl ions reduction, chromium species could be reduced by ($[ZnO_3.V_o^\bullet]$), resulting in di-ionized oxygen vacancies ($[ZnO_3.V_o^{\bullet\bullet}]$) and **¡Error! Nombre de archivo no especificado.** species (Figure 9C<mark>), as described in the Equations 10 and 11.</mark>

$3[ZnO_3.V_o^\bullet]...$**¡Error! Nombre de archivo no especificado.**

$_{(ads)} \rightarrow 3[ZnO_3.V_o^{\bullet\bullet}]...$**¡Error! Nombre de archivo no especificado.**$_{(ads)}$ (10)

$3[ZnO_3.V_o^{\bullet\bullet}]...$**¡Error! Nombre de archivo no especificado.** $_{(ads)} \rightarrow 3[ZnO_3.V_o^{\bullet\bullet}]$
$+$**¡Error! Nombre de archivo no especificado.** (11)
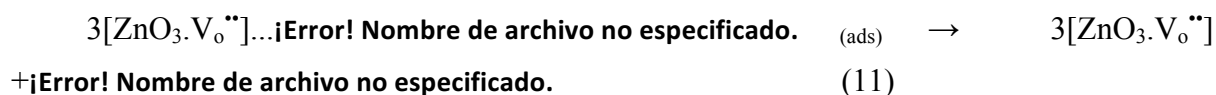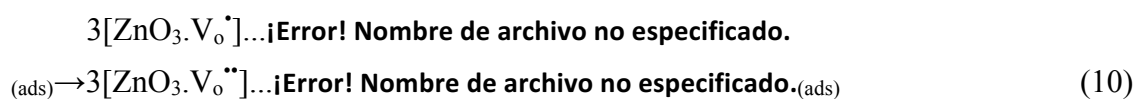
In both situation 1 and 2 (Figure 9B and 9C), the dichromate **¡Error! Nombre de archivo no especificado.**) adsorption process over ZnO active sites allows a Langmuir adsorption process, in which only one layer adsorbed be allowed and, the process does not occur as fast as electron transfer processes, which consequently happen after adsorption. In this way, the adsorption process limits the reaction rate.

Once the pH changed, where was weak acidic (pH=6.0) conditions at <mark>beginning to</mark> neutral conditions (pH=7.5) at the end, it is possible to conclude that the Cr(VI) reduced to Cr(III). Also, the oxide and hydroxide forms of Cr(III) was precipitated as Cr(OH)$_3$ under ZnO surface due tothe negligible Cr(III) observed over the experiments <mark>[91,92]</mark>. It was expected increase in the Cr(III) concentrations in the same acidic pH.

4. Conclusion

In this work, ZnO and ZnO:N samples were obtained through the modified polymeric precursor (MPP) and microwave-assisted hydrothermal (MAH) methods. <mark>The results suggest that the different synthesis methods produce unique physicochemical properties of these materials. MPP and MAH processing conditions methods, such as pH of the precursor solution, play a major role in obtaining different morphologies.</mark> Synthesis method or the doping process do not alter the crystalline phase, which is pure wurtzite ZnO phase. Theoretical Wulff construction obtained through the surface energies shows that MAH samples growth through c-direction, resulting in nanorods morphology, which is dissimilar of MPP samples that present nanoplates morphology. Present results clearly reveal an important strategy that theoretical

simulations constitute to explore experimental conditions. Doping effect produces different modifications in RhB degradation for each synthesis method. For MAH samples, the proposed doping process is not adequate in N quantity to influence, in a positive way, the photocatalytic activity. However, for MPP samples, the same doping method proposed, depicts the higher photocatalytic efficiency. Then, the comprehension of synthesis features on the photocatalytic efficiency of ZnO:N samples shows that other effects – such as facet exposition and morphology – may be more influent than doping itself, despite this is actually efficient depending on the other materials parameters. The correlation with crystal surface exposition and photocatalytic activity was proved by RhB discoloration, under UV and visible illumination. MAH samples present a slightly RhB discoloration as Cr (VI) reduction, compared with MPP samples. ZnOm sample presents better results in RhB discoloration, due to more elevated SSA, crystal face exposition of (002), which present higher photocatalytic activity, and the adequate charge carrier separation, promoted by crystal structure presented. Even the N doping does not affect the band gap values of samples (MPP samples 3.12 eV, MAH samples 3.22 eV), the N doping alters UV and visible photocatalytic activity, due especially to charge recombination rates, dye degradation mechanism and Cr (VI) reduction mechanism. These results show a favorable fabrication technique for a fast and easy photocatalysts production for the efficient removal of pollutants and open new fields of rational design that will benefit the development of novel complex functional materials with desired features and functions.

[1]   A. Manekkathodi, M.Y. Lu, C.W. Wang, L.J. Chen, Direct growth of aligned zinc oxide nanorods on paper substrates for low-cost flexible electronics, Adv. Mater. 22 (2010) 4059–4063. doi:10.1002/adma.201001289.

[2]   H. Zeng, G. Duan, Y. Li, S. Yang, X. Xu, W. Cai, Blue luminescence of ZnO nanoparticles based on non-equilibrium processes: Defect origins and emission controls, Adv. Funct. Mater. 20 (2010) 561–572. doi:10.1002/adfm.200901884.

[3]   Y. Qin, Y. Qin, X. Wang, X. Wang, Z.L. Wang, Z.L. Wang, Microfibre-nanowire hybrid structure for energy scavenging, Nature. 451 (2008) 809–13. doi:10.1038/nature06601.

[4]   Z.L. Wang, J. Song, Piezoelectric Nanogenerators Based on Zinc Oxide Nanowire Arrays, Science (80-.). 312 (2006) 242–246. doi:10.1126/science.1124005.

[5]   P. Yang, H. Yan, S. Mao, R. Russo, J. Johnson, R. Saykally, N. Morris, J. Pham, R. He, H.-J. Choi, Controlled Growth of ZnO Nanowires and Their Optical Properties, Adv. Funct. Mater. 12 (2002) 323–331. doi:10.1002/1616-3028(20020517)12:5<323::AID-ADFM323>3.0.CO;2-G.

[6]   F.A. La Porta, J. Andres, M.V.G. Vismara, C.F.O. Graeff, J.R. Sambrano, M.S. Li, J.A. Varela, E. Longo, Correlation between structural and electronic order-disorder effects and optical properties in ZnO nanocrystals, J. Mater. Chem. C. 2 (2014) 10164–10174. doi:10.1039/C4TC01248H.

[7]   X. Li, Y. Huang, L. Xu, L. Liu, Y. Wang, X. Cao, C. Meng, Z. Wang, Effect of powder size on the microstructure and dielectric properties of ZnO ceramics, Mater. Res. Bull. 68 (2015) 87–91. doi:10.1016/j.materresbull.2015.03.049.

[8]   X.G. Han, H.Z. He, Q. Kuang, X. Zhou, X.H. Zhang, T. Xu, Z.X. Xie, L.S. Zheng, Controlling morphologies and tuning the related properties of nano/microstructured ZnO crystallites, J. Phys. Chem. C. 113 (2009) 584–589. doi:10.1021/jp808233e.

[9]   T. Dixit, A. Kumar, I.A. Palani, V. Singh, Surface-plasmon-mediated red and near infrared emission from Au-coated ZnO/ZnCr2O4 nanocomposites, Scr. Mater. 114 (2016) 84–87. doi:10.1016/j.scriptamat.2015.11.025.

[10]   H. Liu, G. Zhang, J. Yin, J. Liang, W. Sun, Z. Shen, Fabrication of ZnO nanostructures sensitized with CdS quantum dots for photovoltaic application using a convenient solution method, Mater. Res. Bull. 61 (2015) 492–498. doi:10.1016/j.materresbull.2014.10.068.

[11]   M. Birkholz, B. Selle, F. Fenske, W. Fuhs, Structure-function relationship between preferred orientation of crystallites and electrical resistivity in thin

polycrystalline ZnO:Al films, Phys. Rev. B. 68 (2003) 205414. doi:10.1103/PhysRevB.68.205414.

[12]   M. Navaneethan, J. Archana, Y. Hayakawa, Morphological evolution of monodispersed ZnO nanorods to 3 dimensional hierarchical flowers by hydrothermal growth, CrystEngComm. 15 (2013) 8246. doi:10.1039/c3ce41601a.

[13]   D. Pradhan, K.T. Leung, Vertical Growth of Two-Dimensional Zinc Oxide Nanostructures on ITO-Coated Glass: Effects of Deposition Temperature and Deposition Time, J. Phys. Chem. C. 112 (2008) 1357–1364. doi:10.1021/jp076890n.

[14]   Q. Wei, G. Meng, X. An, Y. Hao, L. Zhang, Temperature-controlled growth of ZnO nanostructures: branched nanobelts and wide nanosheets, Nanotechnology. 16 (2005) 2561–2566. doi:10.1088/0957-4484/16/11/016.

[15]   B. Cheng, W. Shi, J.M. Russell-Tanner, L. Zhang, E.T. Samulski, Synthesis of variable-aspect-ratio, single-crystalline ZnO nanostructures., Inorg. Chem. 45 (2006) 1208–14. doi:10.1021/ic051786a.

[16]   N. Wang, X. Cao, Q. Wu, R. Zhang, L. Wang, P. Yin, L. Guo, Hexagonal ZnO Bipyramids: Synthesis, Morphological Evolution, and Optical Properties, J. Phys. Chem. C. 113 (2009) 21471–21476. doi:10.1021/jp9031157.

[17]   M. Pirhashemi, A. Habibi-Yangjeh, Ultrasonic-assisted preparation of plasmonic ZnO/Ag/Ag2WO4 nanocomposites with high visible-light photocatalytic performance for degradation of organic pollutants, J. Colloid Interface Sci. 491 (2017) 216–229. doi:10.1016/j.jcis.2016.12.044.

[18]   K. Ocakoglu, S.A. Mansour, S. Yildirimcan, A.A. Al-Ghamdi, F. El-Tantawy, F. Yakuphanoglu, Microwave-assisted hydrothermal synthesis and characterization of ZnO nanorods, Spectrochim. Acta Part A Mol. Biomol. Spectrosc. 148 (2015) 362–368. doi:10.1016/j.saa.2015.03.106.

[19]   A.P. de Moura, R.C. Lima, M.L. Moreira, D.P. Volanti, J.W.M. Espinosa, M.O. Orlandi, P.S. Pizani, J.A. Varela, E. Longo, ZnO architectures synthesized by a microwave-assisted hydrothermal method and their photoluminescence properties, Solid State Ionics. 181 (2010) 775–780. doi:10.1016/j.ssi.2010.03.013.

[20]   B. Krishnakumar, T. Imae, Chemically modified novel pamam-zno nanocomposite: Synthesis, characterization and photocatalytic activity, Appl. Catal. A Gen. 486 (2014) 170–175. doi:10.1016/j.apcata.2014.08.010.

[21]   R. Velmurugan, K. Selvam, B. Krishnakumar, M. Swaminathan, An efficient reusable and antiphotocorrosive nano ZnO for the mineralization of Reactive Orange 4

under UV-A light, Sep. Purif. Technol. 80 (2011) 119–124. doi:10.1016/j.seppur.2011.04.018.

[22]   J.A. Gerbec, D. Magana, A. Washington, G.F. Strouse, Microwave-enhanced reaction rates for nanoparticle synthesis, J. Am. Chem. Soc. 127 (2005) 15791–15800. doi:10.1021/ja052463g.

[23]   V.R. Shinde, T.P. Gujar, T. Noda, D. Fujita, A. Vinu, M. Grandcolas, J. Ye, Growth of shape- and size-selective zinc oxide nanorods by a microwave-assisted chemical bath deposition method: Effect on photocatalysis properties, Chem. - A Eur. J. 16 (2010) 10569–10575. doi:10.1002/chem.200903370.

[24]   A. Lagashetty, V. Havanoor, S. Basavaraja, S.D. Balaji, A. Venkataraman, Microwave-assisted route for synthesis of nanosized metal oxides, Sci. Technol. Adv. Mater. 8 (2007) 484–493. doi:10.1016/j.stam.2007.07.001.

[25]   I. Bilecka, M. Niederberger, Microwave chemistry for inorganic nanomaterials synthesis., Nanoscale. 2 (2010) 1358–1374. doi:10.1039/b9nr00377k.

[26]   R.N. Gayen, R. Paul, Nano-Structures & Nano-Objects Phosphorous doping in vertically aligned ZnO nanorods grown by wet-chemical method, (2016) 1–7.

[27]   C. Yu, K. Yang, Y. Xie, Q. Fan, J.C. Yu, Q. Shu, C. Wang, Novel hollow Pt-ZnO nanocomposite microspheres with hierarchical structure and enhanced photocatalytic activity and stability., Nanoscale. 5 (2013) 2142–51. doi:10.1039/c2nr33595f.

[28]   C. Yu, W. Zhou, H. Liu, Y. Liu, D.D. Dionysiou, Design and fabrication of microsphere photocatalysts for environmental purification and energy conversion, Chem. Eng. J. 287 (2016) 117–129. doi:10.1016/j.cej.2015.10.112.

[29]   J.M. Bian, X.M. Li, C.Y. Zhang, L.D. Chen, Q. Yao, Synthesis and characterization of two-layer-structured ZnO p-n homojunctions by ultrasonic spray pyrolysis, Appl. Phys. Lett. 84 (2004) 3783–3785. doi:10.1063/1.1739280.

[30]   A. Tsukazaki, A. Ohtomo, T. Onuma, M. Ohtani, T. Makino, M. Sumiya, K. Ohtani, S.F. Chichibu, S. Fuke, Y. Segawa, H. Ohno, H. Koinuma, M. Kawasaki, Repeatedd temperature modulation epitaxy for p-type doping and light-emitting diode based on ZnO, Nat. Mater. 4 (2005) 42–46. doi:10.1002/adma.200502633.

[31]   H. ~W. Liang, Y. ~M. Lu, D. ~Z. Shen, Y. ~C. Liu, J. ~F. Yan, C. ~X. Shan, B. ~H. Li, Z. ~Z. Zhang, J. ~Y. Zhang, X. ~W. Fan, P-type ZnO thin films prepared by plasma molecular beam epitaxy using radical NO, Phys. Status Solidi Appl. Res. 202 (2005) 1060–1065. doi:10.1002/pssa.200420012.

[32] K.C. Pradel, W. Wu, Y. Zhou, X. Wen, Y. Ding, Z.L. Wang, Piezotronic effect in solution-grown p-type ZnO nanowires and films, Nano Lett. 13 (2013) 2647–2653. doi:10.1021/nl400792w.

[33] M. Suja, S.B. Bashar, M.M. Morshed, J. Liu, Realization of Cu-Doped p-Type ZnO Thin Films by Molecular Beam Epitaxy., ACS Appl. Mater. Interfaces. 7 (2015) 8894–9. doi:10.1021/acsami.5b01564.

[34] T.M. Barnes, K. Olson, C.A. Wolden, On the formation and stability of p-type conductivity in nitrogen-doped zinc oxide, Appl. Phys. Lett. 86 (2005) 1–3. doi:10.1063/1.1884747.

[35] X. Chen, Z. Zhang, B. Yao, M. Jiang, S. Wang, B. Li, C. Shan, L. Liu, D. Zhao, D. Shen, Effect of compressive stress on stability of N-doped p-type ZnO, Appl. Phys. Lett. 99 (2011). doi:10.1063/1.3631677.

[36] S. Sun, X. Chang, X. Li, Z. Li, Synthesis of N-doped ZnO nanoparticles with improved photocatalytical activity, Ceram. Int. 39 (2013) 5197–5203. doi:10.1016/j.ceramint.2012.12.018.

[37] C. Wu, Facile one-step synthesis of N-doped ZnO micropolyhedrons for efficient photocatalytic degradation of formaldehyde under visible-light irradiation, Appl. Surf. Sci. 319 (2014) 237–243. doi:10.1016/j.apsusc.2014.04.217.

[38] E.S. Tuzemen, K. Kara, S. Elagoz, D.K. Takci, I. Altuntas, R. Esen, Structural and electrical properties of nitrogen-doped ZnO thin films, in: Appl. Surf. Sci., 2014: pp. 157–163. doi:10.1016/j.apsusc.2014.02.118.

[39] D.Z. Zhou, B. Li, H.L. Wang, M. Salik, H.H. Wu, Z.F. Hu, S. Gao, Y.F. Peng, L.X. Yi, X.Q. Zhang, Y.S. Wang, Fabrication and electrical characterization of Li-N dual doped ZnO thin film transistor, Appl. Surf. Sci. 305 (2014) 474–476. doi:10.1016/j.apsusc.2014.03.116.

[40] D. Zhang, J. Gong, J. Ma, G. Han, Z. Tong, A facile method for synthesis of N-doped ZnO mesoporous nanospheres and enhanced photocatalytic activity., Dalton Trans. 42 (2013) 16556–61. doi:10.1039/c3dt52039k.

[41] X. Zong, C. Sun, H. Yu, Z.G. Chen, Z. Xing, D. Ye, G.Q. Lu, X. Li, L. Wang, Activation of photocatalytic water oxidation on N-doped ZnO bundle-like nanoparticles under visible light, J. Phys. Chem. C. 117 (2013) 4937–4942. doi:10.1021/jp311729b.

[42] C.H. Park, S.B. Zhang, S.-H. Wei, Origin of p-type doping difficulty in ZnO: The impurity perspective, Phys. Rev. B. 66 (2002) 73202. doi:10.1103/PhysRevB.66.073202.

[43]   A. El-Amiri, H. Lassri, E.K. Hlil, M. Abid, Explanation of ferromagnetism origin in N-doped ZnO by first principle calculations, J. Magn. Magn. Mater. 374 (2015) 338–341. doi:10.1016/jommm.2014.08.068.

[44]   M. Naouar, I. Ka, M. Gaidi, H. Alawadhi, B. Bessais, M.A. El Khakani, Growth, structural and optoelectronic properties tuning of nitrogen-doped ZnO thin films synthesized by means of reactive pulsed laser deposition, Mater. Res. Bull. 57 (2014) 47–51. doi:10.1016/j.materresbull.2014.05.020.

[45]   S.H. Park, J.H. Chang, T. Minegishi, J.S. Park, I.H. Im, M. Ito, T. Taishi, S.K. Hong, D.C. Oh, M.W. Cho, T. Yao, Investigation on the ZnO:N films grown on (0001) and (000$\bar{1}$) ZnO templates by plasma-assisted molecular beam epitaxy, J. Cryst. Growth. 311 (2009) 2167–2171. doi:10.1016/j.jcrysgro.2008.11.018.

[46]   L.-C. Chao, J.-W. Chen, H.-C. Peng, C.-H. Ho, Characterization of nitrogen doped p-type ZnO thin films prepared by reactive ion beam sputter deposition, Surf. Coatings Technol. 231 (2013) 492–495. doi:10.1016/j.surfcoat.2012.10.077.

[47]   C. Wang, Z. Ji, J. Xi, J. Du, Z. Ye, Fabrication and characteristics of the low-resistive p-type ZnO thin films by DC reactive magnetron sputtering, Mater. Lett. 60 (2006) 912–914. doi:10.1016/j.matlet.2005.10.057.

[48]   Z. Wang, Y. Yue, Y. Cao, Preparation and properties of nitrogen doped p-type zinc oxide films by reactive magnetron sputtering, Vacuum. 101 (2014) 313–316. doi:10.1016/j.vacuum.2013.10.001.

[49]   H. Lu, P. Zhou, H. Liu, L. Zhang, Y. Yu, Y. Li, Z. Wang, Effects of nitrogen and oxygen partial pressure on the structural and optical properties of ZnO:N thin films prepared by magnetron sputtering, Mater. Lett. 165 (2016) 123–126. doi:10.1016/j.matlet.2015.11.105.

[50]   N.P. Herring, L.S. Panchakarla, M.S. El-Shall, P-Type nitrogen-Doped ZnO nanostructures with controlled shape and doping level by facile microwave synthesis, Langmuir. 30 (2014) 2230–2240. doi:10.1021/la404593w.

[51]   V.R. de Mendonça, C. Ribeiro, Influence of TiO2 morphological parameters in dye photodegradation: A comparative study in peroxo-based synthesis, Appl. Catal. B Environ. 105 (2011) 298–305. doi:10.1016/j.apcatb.2011.04.018.

[52]   I.M.P. Silva, G. Byzynski, C. Ribeiro, E. Longo, Different dye degradation mechanisms for ZnO and ZnO doped with N (ZnO:N), J. Mol. Catal. A Chem. 417 (2016) 89–100. doi:http://dx.doi.org/10.1016/j.molcata.2016.02.027.

[53]   H. Sudrajat, S. Babel, Comparison and mechanism of photocatalytic activities of N-ZnO and N-ZrO2 for the degradation of rhodamine 6G, Environ. Sci. Pollut. Res. 23 (2016) 10177–10188. doi:10.1007/s11356-016-6191-6.

[54]   M. Shekofteh-Gohari, A. Habibi-Yangjeh, Ternary ZnO/Ag3VO4/Fe3O4 nanocomposites: Novel magnetically separable photocatalyst for efficiently degradation of dye pollutants under visible-light irradiation, Solid State Sci. 48 (2015) 177–185. doi:10.1016/j.solidstatesciences.2015.08.010.

[55]   M. Shekofteh-Gohari, A. Habibi-Yangjeh, Novel magnetically separable ZnO/AgBr/Fe 3 O 4 /Ag 3 VO 4 nanocomposites with tandem n–n heterojunctions as highly efficient visible-light-driven photocatalysts, RSC Adv. 6 (2016) 2402–2413. doi:10.1039/C5RA21356H.

[56]   M. Pirhashemi, A. Habibi-Yangjeh, Photosensitization of ZnO by AgBr and Ag2CO3: Nanocomposites with tandem n-n heterojunctions and highly enhanced visible-light photocatalytic activity, J. Colloid Interface Sci. 474 (2016) 103–113. doi:10.1016/j.jcis.2016.04.022.

[57]   H. He, S. Xue, Z. Wu, C. Yu, K. Yang, G. Peng, W. Zhou, D. Li, Sonochemical fabrication, characterization and enhanced photocatalytic performance of Ag2S/Ag2WO4 composite microrods, Chinese J. Catal. 37 (2016) 1841–1850. doi:10.1016/S1872-2067(16)62515-9.

[58]   Elson Longo da Silva; José Arana Varela; David Keyson de Araújo Almeida; Diogo Paschoalini Volanti, E. Longo Da Silva, J. Arana Varela, D.K. De Araujo Almeida, D. Paschoalini Volanti, Aided Device for Hydrothermal Synthesis of Nanostructured Oxides, Particularly Obtaining Particles of Metal Oxides, Comprises Container, in which Hydrothermal Reaction Takes Place, and Lid for Container, BR200815393-A2, 2010.

[59]   G. Wulff, Zur Frage der Geschwindigkeit des Wachstums und der Auflösung der Krystallflächen, Zeitschrift Für Kryst. Und Mineral. 34 (1901) 449–530. doi:10.1524/zkri.1901.34.1.449.

[60]   S. Na, C. Park, P. Chul-Hong, First-Principles Study of the Surface Energy and Atom Cohesion of Wurtzite ZnO and ZnS - Implications for Nanostructure Formation, J. Korean Phys. Soc. 56 (2010) 498. doi:10.3938/jkps.56.498.

[61]   J. Andrés, L. Gracia, A.F. Gouveia, M.M. Ferrer, E. Longo, Effects of surface stability on the morphological transformation of metals and metal oxides as investigated by first-principles calculations., Nanotechnology. 26 (2015) 405703. doi:10.1088/0957-4484/26/40/405703.

[62] M.L. Moreira, V.M. Longo, W. Avansi, M.M. Ferrer, J. Andrés, V.R. Mastelaro, J.A. Varela, É. Longo, Quantum Mechanics Insight into the Microwave Nucleation of SrTiO3 Nanospheres, J. Phys. Chem. C. 116 (2012) 24792–24808. doi:10.1021/jp306638r.

[63] K. Momma, F. Izumi, VESTA 3 for three-dimensional visualization of crystal, volumetric and morphology data, J. Appl. Crystallogr. 44 (2011) 1272–1276. doi:10.1107/S0021889811038970.

[64] APHA/AWWA/WEF, Standard Methods for the Examination of Water and Wastewater, 2012. doi:ISBN 9780875532356.

[65] F. Ahmed, S. Kumar, N. Arshi, M.S. Anwar, B. Heun Koo, Morphological evolution between nanorods to nanosheets and room temperature ferromagnetism of Fe-doped ZnO nanostructures, CrystEngComm. 14 (2012) 4016. doi:10.1039/c2ce25227a.

[66] Y. V Kaneti, Z. Zhang, J. Yue, Q.M.D. Zakaria, C. Chen, X. Jiang, A. Yu, Crystal plane-dependent gas-sensing properties of zinc oxide nanostructures: experimental and theoretical studies., Phys. Chem. Chem. Phys. 16 (2014) 11471–80. doi:10.1039/c4cp01279h.

[67] S. Cho, S.-H. Jung, K.-H. Lee, Morphology-Controlled Growth of ZnO Nanostructures Using Microwave Irradiation: from Basic to Complex Structures, J. Phys. Chem. C. 112 (2008) 12769–12776. doi:10.1021/jp803783s.

[68] J. Ananpattarachai, S. Seraphin, P. Kajitvichyanukul, Formation of hydroxyl radicals and kinetic study of 2-chlorophenol photocatalytic oxidation using C-doped TiO2, N-doped TiO2, and C,N Co-doped TiO2 under visible light, Environ. Sci. Pollut. Res. 23 (2016) 3884–3896. doi:10.1007/s11356-015-5570-8.

[69] G.B. Soares, B. Bravin, C.M.P. Vaz, C. Ribeiro, Facile synthesis of N-doped TiO2 nanoparticles by a modified polymeric precursor method and its photocatalytic properties, Appl. Catal. B Environ. 106 (2011) 287–294. doi:10.1016/j.apcatb.2011.05.018.

[70] Z. Yu, L.-C. Yin, Y. Xie, G. Liu, X. Ma, H.-M. Cheng, Crystallinity-dependent substitutional nitrogen doping in ZnO and its improved visible light photocatalytic activity., J. Colloid Interface Sci. 400 (2013) 18–23. doi:10.1016/j.jcis.2013.02.046.

[71] Y.K. Gao, F. Traeger, C. Wöll, H. Idriss, Glycine adsorption and photo-reaction over ZnO(000ī) single crystal, Surf. Sci. 624 (2014) 112–117. doi:10.1016/j.susc.2014.02.002.

[72]   A. Jilani, J. Iqbal, S. Rafique, M.S. Abdel-wahab, Y. Jamil, A.A. Al-Ghamdi, Morphological, optical and X-ray photoelectron chemical state shift investigations of ZnO thin films, Opt. - Int. J. Light Electron Opt. 127 (2016) 6358–6365. doi:10.1016/j.ijleo.2016.04.127.

[73]   X.-J. Lv, S. Zhou, X. Huang, C. Wang, W.-F. Fu, Photocatalytic overall water splitting promoted by SnOx–NiGa2O4 photocatalysts, Appl. Catal. B Environ. 182 (2016) 220–228. doi:10.1016/j.apcatb.2015.09.032.

[74]   K. Rajeshwar, Fundamentals of Semiconductors Electrochemistry and Photoelectrochemistry, Encycl. Electrochem. (2007) 1–51. doi:10.1002/9783527610426.bard060001.

[75]   C. Di Valentin, E. Finazzi, G. Pacchioni, A. Selloni, S. Livraghi, M.C. Paganini, E. Giamello, N-doped TiO2: Theory and experiment, Chem. Phys. 339 (2007) 44–56. doi:10.1016/j.chemphys.2007.07.020.

[76]   J. Arul Mary, J. Judith Vijaya, M. Bououdina, L. John Kennedy, J.H. Daie, Y. Song, Investigation of structural, surface morphological, optical properties and first-principles study on electronic and magnetic properties of (Ce, Fe)-co doped ZnO, Phys. B Condens. Matter. 456 (2015) 344–354. doi:10.1016/j.physb.2014.09.023.

[77]   S.-Y. Pung, W.-P. Lee, A. Aziz, Kinetic Study of Organic Dye Degradation Using ZnO Particles with Different Morphologies as a Photocatalyst, Int. J. Inorg. Chem. 2012 (2012) 1–9. doi:10.1155/2012/608183.

[78]   A.M. Ali, E.A.C. Emanuelsson, D.A. Patterson, Photocatalysis with nanostructured zinc oxide thin films: The relationship between morphology and photocatalytic activity under oxygen limited and oxygen rich conditions and evidence for a Mars Van Krevelen mechanism, Appl. Catal. B Environ. 97 (2010) 168–181. doi:10.1016/j.apcatb.2010.03.037.

[79]   C. Yu, F. Cao, X. Li, G. Li, Y. Xie, J.C. Yu, Q. Shu, Q. Fan, J. Chen, Hydrothermal synthesis and characterization of novel PbWO4 microspheres with hierarchical nanostructures and enhanced photocatalytic performance in dye degradation, Chem. Eng. J. 219 (2013) 86–95. doi:10.1016/j.cej.2012.12.064.

[80]   H. Qin, W. Li, Y. Xia, T. He, Photocatalytic activity of heterostructures based on ZnO and N-doped ZnO, ACS Appl. Mater. Interfaces. 3 (2011) 3152–3156. doi:10.1021/am200655h.

[81]   M. Samadi, M. Zirak, A. Naseri, E. Khorashadizade, A.Z. Moshfegh, Recent progress on doped ZnO nanostructures for visible-light photocatalysis, Thin Solid Films. (2016). doi:10.1016/j.tsf.2015.12.064.

[82]   T. Tan, D. Beydoun, R. Amal, Effects of organic hole scavengers on the photocatalytic reduction of selenium anions, J. Photochem. Photobiol. A Chem. 159 (2003) 273–280. doi:10.1016/S1010-6030(03)00171-0.

[83]   J. Ma, Degradation of atrazine by manganese-catalysed ozonationâ€"influence of radical scavengers, Water Res. 34 (2000) 3822–3828. doi:10.1016/S0043-1354(00)00130-5.

[84]   S. Rengaraj, X.Z. Li, Enhanced photocatalytic reduction reaction over Bi3+-TiO2 nanoparticles in presence of formic acid as a hole scavenger, Chemosphere. 66 (2007) 930–938. doi:10.1016/j.chemosphere.2006.06.007.

[85]   S.H. Cho, H.H. Nguyen, G. Gyawali, J.-E. Son, T. Sekino, B. Joshi, S.H. Kim, Y.H. Jo, T.H. Kim, S.W. Lee, Effect of microwave-assisted hydrothermal process parameters on formation of different TiO2 nanostructures, Catal. Today. 266 (2016) 46–52. doi:10.1016/j.cattod.2015.10.001.

[86]   U. Riaz, S.M. Ashraf, V. Budhiraja, S. Aleem, J. Kashyap, Comparative studies of the photocatalytic and microwave –assisted degradation of alizarin red using ZnO/poly(1- naphthylamine) nanohybrids, J. Mol. Liq. 216 (2016) 259–267. doi:10.1016/j.molliq.2016.01.018.

[87]   R.J. Kieber, G.R. Helz, Indirect photoreduction of aqueous chromium(VI), Environ. Sci. Technol. 26 (1992) 307–312. doi:10.1021/es00026a010.

[88]   D. Shao, X. Wang, Q. Fan, Photocatalytic reduction of Cr(VI) to Cr(III) in solution containing ZnO or ZSM-5 zeolite using oxalate as model organic compound in environment, Microporous Mesoporous Mater. 117 (2009) 243–248. doi:10.1016/j.micromeso.2008.06.026.

[89]   X. Song, Y. Liu, Y. Zheng, K. Ding, S. Nie, P. Yang, Synthesis of butterfly-like ZnO nanostructures and study of their self-reducing ability toward Au(3+) ions for enhanced photocatalytic efficiency., Phys. Chem. Chem. Phys. 18 (2016) 4577–84. doi:10.1039/c5cp07187a.

[90]   B.Z. Wei Song, Yanfei Wang, Hailong Hu, Fabrication of surface-enhanced Raman scaterring-active ZnO/Ag composite microspheres, J. Raman Spectrosc. 38 (2007) 1538–1553. doi:10.1002/jrs.

[91]   C.-C. Wang, X.-D. Du, J. Li, X.-X. Guo, P. Wang, J. Zhang, Photocatalytic Cr(VI) reduction in metal-organic frameworks: A mini-review, Appl. Catal. B Environ. 193 (2016) 198–216. doi:10.1016/j.apcatb.2016.04.030.

[92]   D. a Skoog, D.M. West, F.J. Holler, S.R. Crouch, Fundamentals of Analytical Chemistry, Anal. Chem. 398 (2004) 27–28. doi:10.1007/s00216-010-3971-6.